Available online at www.sciencedirect.com

jmr&t Journal of Materials Research and Technology

www.jmrt.com.br

Original Article

Sisal cellulose and magnetite nanoparticles: formation and properties of magnetic hybrid films

Daiana M. Furlan[a], *Daniella Lury Morgado*[a], *Adilson J.A. de Oliveira*[b], *Ângelo D. Faceto*[b], *Daniel A. de Moraes*[c], *Laudemir C. Varanda*[c], *Elisabete Frollini*[a,*]

[a] *Macromolecular Materials and Lignocellulosic Fibers Group, Center for Research on Science and Technology of BioResources, Institute of Chemistry of São Carlos, University of São Paulo, São Carlos, São Paulo, Brazil*

[b] *Physics Department, Federal University of São Carlos, São Carlos, São Paulo, Brazil*

[c] *Colloidal Materials Group, Center for Research on Science and Technology of BioResources, Institute of Chemistry of São Carlos, University of São Paulo, São Carlos, São Paulo, Brazil*

ARTICLE INFO

Article history:
Received 7 September 2018
Accepted 28 February 2019
Available online 8 April 2019

Keywords:
Sisal cellulose
Magnetite nanoparticles
Magnetic hybrid films

ABSTRACT

In this study, sisal cellulose/magnetite-nanoparticle (Fe_3O_4 NPs; 0.5, 1.4, and 3.0 g L^{-1}) hybrid films (denoted as **FCFe$_{0.5}$**, **FCFe$_{1.4}$**, and **FCFe$_{3.0}$**, respectively) were prepared by casting, using the solvent system LiCl/DMAc. Sisal was chosen as a cellulose source because it is a fast-growing plant, in contrast to the long cycle of woody trees, and Brazil accounts for most of the sisal produced in the world. Fe_3O_4 NPs were chosen owing to their excellent properties (superparamagnetic behavior at room temperature, high chemical stability, and low toxicity). The synthesized magnetite NPs (coated with oleic acid and oleylamine to prevent agglomeration during synthesis) were spherical with an average diameter of 5.1 ± 0.5 nm (transmission electron microscopy analysis; TEM). X-ray diffraction analysis showed that the NPs were satisfactorily incorporated into the cellulose films (as confirmed by TEM) and that their presence favored the formation of cellulose crystalline domains. FCFe$_{1.4}$ and FCFe$_{3.0}$ exhibited higher tensile strengths (14.3 MPa and 12.1 MPa, respectively) than the neat cellulose film (9.9 MPa). The moduli of elasticity of FCFe$_{0.5}$, FCFe$_{1.4}$, and FCFe$_{3.0}$ were 1650, 1500 MPa, and 780 MPa, respectively, lower than that of the cellulose film (1860 MPa), indicating that the incorporation of NPs in the cellulosic matrix decreased the films' stiffness. Hybrid films exhibited high magnetizations at 300 K, i.e., 23.0 emu g^{-1} (FCFe$_{0.5}$), 31.0 emu g^{-1} (FCFe$_{1.4}$), and 37.0 emu g^{-1} (FCFe$_{3.0}$), as well as no magnetic hysteresis and remanent magnetization (Mr) null, namely, a superparamagnetic behavior at room temperature. The results obtained suggest several applications of hybrid films based on cellulose and magnetite, such as biomedical applications, miniaturized electronic devices, and advanced catalysis.

* *Corresponding author.*
E-mail: elisabete@iqsc.usp.br (E. Frollini).

https://doi.org/10.1016/j.jmrt.2019.02.005

1. Introduction

The sustainable use of biomass and its recovery to convert it into profitable products and materials require effort, mainly with regard to its exploration in applications different from those already considered. In this scenario, cellulosic compounds emerge as some of the most important raw materials to consider.

Cellulose is the most abundant natural polymer obtained from renewable sources, including jute, ramie, sisal, sugarcane, and cotton. Sisal, as the other plants mentioned, is a source with fast growth and regeneration cycle. Also, the world's largest producer of sisal is Brazil, and these aspects led to the choice of this fiber as a source of cellulose in the present study [1–5]. The chemical structure of cellulose differs from those of many synthetic polymers owing to its hydrophilic character, stereoregularity, and polyfunctionality [6]. These characteristics, combined with its low cost, make cellulosic pulp very attractive for use as starting material in the preparation of new materials and composites [7], cellulose nanofibril hydrogel [8], microcapsules containing cellulose nanofibrils [9], and organic–inorganic hybrids, such as those considered in this study.

Magnetic nanoparticles (MNPs) can be incorporated into different materials, allowing the creation of end-products with diverse properties, besides magnetic properties [10,11]. Composites consisting of MNPs and cellulose have attracted great interest owing to the synergy between the properties derived from the individual components. This type of hybrid material may exhibit different structural and functional properties, as it also represents a new concept material with advantages such as biocompatibility and biodegradability [12–16]. Moreover, the dispersion of magnetic nanoparticles (MNPs) in an organic polymer to form magnetic composites may improve its optical, mechanical, and other properties [17]. Several applications can be envisaged for cellulose–MNP materials, such as conductive paper [18], nanocatalysts for removal of textile dyes [19], catalytic and antibacterial activities [20], and transparent films for magneto-optical applications [21].

Iron oxides, in particular magnetite (Fe_3O_4), represent the magnetic particles that are most commonly associated with a polymer matrix in a nanometric scale owing to their excellent magnetic properties, such as superparamagnetic behavior at room temperature, high chemical stability, exceptional biocompatibility of their surfaces [22], low toxicity compared to both metals or other metal-oxide NPs, and the facility and low cost of the procedures available for their preparation [23].

Cellulosic materials have been used for the preparation of materials containing an organic–inorganic interface, in the form of fibers, films, and microspheres [12–14]. Hybrid films obtained by mixing the magnetic component with a cellulose derivative, namely, cellulose acetate, have been reported by Shim et al. [24]. However, the number of studies related to obtaining magnetic composite films from underivatized cellulose is still small [25], mainly because cellulose dissolves in a limited number of solvents. In this context, herein we prepared sisal cellulose/Fe_3O_4-nanoparticle (FCFe) hybrid films by casting, using LiCl/DMAc as the solvent system. The influence of different amounts of MNPs on the properties of cellulose films (FCs) was evaluated, with the aim of preparing cellulosic films with enhanced mechanical and magnetic properties.

2. Materials and methods

2.1. Materials

Sisal pulp was provided by the Lwarcel Company (Lençois Paulista, São Paulo, Brazil), where it was obtained by the *Kraft* pulping process, using an elemental chlorine-free bleaching sequence [25]. Lithium chloride (LiCl, Synth), *N*,*N*-dimethylacetamide (DMAc, Vetec), sodium hydroxide, ethanol, methanol, and hexane (Synth), cupriethylenediamine (Qeel), 1,2-hexadecanodiol, benzyl ether, oleic acid, oleylamine, and iron (III) acetylacetonate (Sigma-Aldrich) were used without further purification—except for DMAc, which was purified by distillation with CaH_2, followed by storage over 4 Å molecular sieves, and for LiCl, which was dried under vacuum overnight at 60 °C and stored in a desiccator before use.

The properties of the sisal pulp (viscometric degree of polymerization = 723 (DPv), crystallinity = 70%, and α-cellulose = 88.7%) were determined as described elsewhere [26]. Prior to its use, the pulp was treated with NaOH 20% (wt%) solution (mercerization treatment), as previously described [26,27]. The mercerized sisal cellulose was dried at room temperature for 24 h and subsequently in an air-circulating oven at 105 °C until it had a constant weight. The mercerized sisal cellulose exhibited DP_v = 670, crystallinity = 58.0%, and α-cellulose content = 90.5%, which upgraded its quality as a dissolving pulp [1], mainly owing to the decrease in crystallinity.

2.2. Methods

2.2.1. Synthesis of Fe_3O_4 NPs

The superparamagnetic Fe_3O_4 NPs were prepared with the thermal decomposition method in the presence of polyols, following an adapted experimental procedure described previously [28]. In a three-necked round-bottom flask, iron (III) acetylacetonate (1 mmol), 1,2-hexadecanodiol (5 mmol), oleic acid (3 mmol), oleylamine (3 mmol), and benzyl ether (20 mL) were mixed and heated to 100 °C under magnetic stirring for 15 min and a nitrogen flow. The NPs were coated with oleic acid and oleylamine to prevent agglomeration during synthesis. Afterwards, under a blanket of nitrogen, the mixture was heated to 200 °C for 2 h and then subjected to reflux (298 °C) for 1 h. The black-colored mixture was cooled to room temperature by removing the heat source. Under ambient conditions, ethanol and hexane were added to the mixture, and a black material was isolated by centrifuging (9000 rpm, 10 min). This procedure was applied until the complete removal of the undispersed residue, and the resulting material was then redispersed into hexane and stored at room temperature.

2.2.2. Elaboration of films

Cellulose film (FC). The FC was prepared in a LiCl/DMAc solvent system following a previously described experimental procedure [4,26]. Cellulose (1.5 g) and LiCl (1.5 g) were mixed in a

glass reactor equipped with a mechanical stirrer and a vacuum pump. The system was heated to 110 °C and maintained at that temperature for 30 min. Next, 45 mL of DMAc was added, and the vacuum pump was turned off and replaced by a reflux condenser under a flow of nitrogen. The mixture was heated to 160 °C and stirred for 1.5 h, cooled down to room temperature, and allowed to stir overnight to obtain a homogeneous solution. After this period, the solution was immediately cast on glass Petri dishes (diameter 9.6 cm) and left to stand at room temperature until a gel-like substance with the minimal consistency for washing was formed. The material was then exhaustively washed with distilled water until the solvent system was entirely removed. To confirm the complete elimination of LiCl in this step, the conductivity of the washing residue was measured repeatedly until it equaled that of the starting water. The residual water was eliminated by drying the formed film at room temperature for one day, then sandwiching it between two Teflon® plates, and finally drying it at 60 °C under reduced pressure until it had a constant weight.

FCFe hybrid films. The hybrid films were prepared from LiCl/DMAc solutions, following the same procedure as that mentioned for the FC. Fe_3O_4 NPs (dried for one day at room temperature to eliminate hexane) were dispersed in DMAc using an ultrasound bath just before the use of the solvent. A set of the films of cellulose/Fe_3O_4 NPs were prepared by changing the concentration of Fe_3O_4 NPs dispersed in DMAc to 0.5, 1.4, and 3.0 g L^{-1}, and the hybrid films were denoted as **$FCFe_{0.5}$**, **$FCFe_{1.4}$**, and **$FCFe_{3.0}$**, respectively.

2.3. *Characterization of starting materials, FC and FCFe films*

Elemental analysis and atomic absorption. The possible presence of residual solvent system (LiCl/DMAc) in the films was evaluated by elemental analysis (nitrogen content; CE Instruments CHNS-O model EA-1110) and atomic absorption (lithium content; Varian atomic absorption spectrometer model AA240FS). Prior to elemental analysis, the films were sprayed using liquid nitrogen. The atomic absorption analysis was performed via wet dissolution, digesting 4 mg of the dried samples (pure FC or hybrid films) in 1 mL of concentrated H_2SO_4 plus heating, followed by the addition of hydrogen peroxide dropwise until a clear solution was observed. The solution was cooled to room temperature and diluted to a 50-mL volume using a KCl 2 ppm solution.

Crystallinity index (Ic). X-ray diffraction (XRD) analysis was used to evaluate the Ic of cellulose, Fe_3O_4 NP phase formation, and its incorporation into the hybrid films. Measurements were performed using a Rigaku-Denki® RINT2000 diffractometer with a horizontal goniometer of high angle operating at 50 kV/100 mA and a Bruker D8 Advanced diffractometer, both using Cu Kα radiation (λ = 1.542 Å). The diffraction patterns were recorded in the range $2\theta = 10–80°$ and at a scanning speed of 2° min^{-1} and 0.02°/0.2 s, respectively. The Ic of the materials was evaluated as described elsewhere [1,3], using Eq. (1):

$$IC = 1 - \frac{I_1}{I_2} \quad (1)$$

I_1 is the minimum intensity of the noncrystalline part of cellulose (18° for cellulose I and 16° for cellulose II),

I_2 is the maximum intensity of the crystalline part of cellulose ($22° \leq 2\theta \leq 23°$ for cellulose I and $18° \leq 2\theta \leq 22°$ for cellulose II).

Thermogravimetric analysis (TGA). TGA was conducted using a Shimadzu TGA-50 instrument for samples of cellulose, Fe_3O_4 NPs, and the hybrid films. Approximately 5.0 mg of the sample was weighed and heated from room temperature to 800 °C (20 °C min^{-1}) under N_2 flow (50 mL min^{-1}).

The mass percentage of Fe_3O_4 incorporated into the films was determined via TGA under air atmosphere (figures not shown) under the same conditions described above, from the difference of the final masses of **FCFe** and **FC**.

Morphological analysis. The morphology of the films was examined by scanning electron microscopy (SEM) using a LEO 440 ZEISS/LEICA SEM system at an accelerating voltage of 20 kV, equipped with an energy-dispersive X ray spectrometer (EDX; EDX LINK ANALYTICAL, Isis System Series 200). Samples were metalized with gold before examination. SEM images of the surface and of the cross section of the films were assessed. The presence of iron-oxide NPs in the hybrid films was investigated by EDX. The size, shape and particle-size distribution of the Fe_3O_4 NPs were analyzed by transmission electron microscopy (TEM) using a Philips CM120 microscope operating at 120 kV and a JEOL JEM2100 microscope operating at 200 kV. A sample of as-synthesized NPs dispersed in hexane was diluted, sonicated, and then dropped on a Formvar® - and carbon-coated copper grid, and the hybrid films were fragmented, suspended in isopropanol, and dropped onto the sample holder. In both cases, the solvent was slowly evaporated at room temperature and the copper grids remained under vacuum for 12 h. A statistical analysis (average diameter and standard deviation) was performed by counting around 200 NPs using the free software ImageJ version 1.42q.

Tensile strength. The tensile tests were performed using a TA Instruments model DMA Q800 operating in tension-film mode at room temperature, according to the equipment manual instructions for this type of analysis. The film samples were strained at a constant rate of 1 N min^{-1} until 18 N or failure, with a preload of 0.001 N. Samples 5.7 mm in width and 10 mm in gauge length were used for the tests. At least three samples from each film were tested, and the errors concerning the average results reported (section 3.3.5) ranged from ±3 to ±7%.

Magnetic measurements. The hysteresis loops of the Fe_3O_4 NPs and the hybrid films were measured by a vibrating sample magnetometer (VSM; EG&G Princeton Applied Research) at300 K, with a static magnetic field applied parallel to the film. The applied field was systematically varied from −10.0 to 10.0 kOe. Magnetic susceptibility measurements were performed using an MPMS3 from Quantum Design Squid magnetometer. The magnetic susceptibility data of the Fe_3O_4 particles were obtained from field-cooling/zero-field cooling (ZFC) curves by heating the sample from 5 to 300 K with an applied field of 50 Oe. First, the sample was cooled down to 5 K without any applied field to obtain ZFC measurements; then, the data were obtained after cooling down from 300 K to 5 K with an applied field of 50 Oe, i.e., field-cooling protocol.

Table 1 – Nitrogen and lithium contents, determined by elemental analysis and atomic absorption, respectively, for the starting cellulose and films (FC, $FCFe_{0.5}$, $FCFe_{1.4}$, and $FCFe_{3.0}$).

Samples	Nitrogen content (%)	Lithium content ($mg\,L^{-1}$)
Starting cellulose	0.005	<LoD[a]
FC	0.2	0.001
$FCFe_{0.5}$	0.4	0.001
$FCFe_{1.4}$	0.2	0.003
$FCFe_{3.0}$	0.4	0.005

[a] LoD, limit of detection; LoD = 0.001 mg Li L^{-1}.

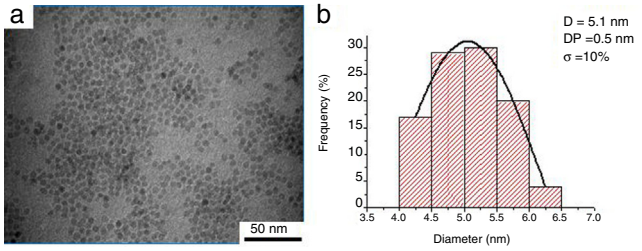

Fig. 1 – (a) TEM images of the as-synthesized magnetite NPs and (b) Gaussian fit of the particle-size distribution of the magnetite.

3. Results and discussion

3.1. *Nitrogen and lithium analyses*

In order to confirm the absence of DMAc, the solvent used in the preparation of the films, the content of nitrogen was evaluated by elemental analysis. Another source of nitrogen in the hybrid films was oleylamine ($C_{18}H_{37}N$), which was added during the synthesis, along with oleic acid, to avoid aggregation of the NPs. The starting sisal cellulose and its film, as well as the hybrid films, were also analyzed by atomic absorption to verify the presence of lithium from residual LiCl, which was used together with DMAc as the solvent system in the preparation of the films (Table 1).

The results showed that the successive washes with distilled water were efficient in promoting the elimination of DMAc, because very small amounts of nitrogen (equal to or less than 0.4%) were found in the films after the washing and drying process. The amounts of nitrogen in the hybrid films may also be assigned to the presence of oleylamine on the surfaces of magnetite NPs, as mentioned. The atomic absorption results showed that practically no lithium residues were found in all samples.

3.2. *TEM*

The average size, shape, and size distribution of the as-synthesized magnetite NPs was investigated by TEM (Fig. 1).

The TEM image (Fig. 1a) indicates that the synthesis of magnetite using the modified polyol method gave rise to spherical NPs with an average diameter of 5.1 ± 0.5 nm. Varanda et al. [29] obtained Fe_3O_4 NPs with 5.0 ± 0.4 nm diameter by employing the same protocol. Owing to the low degree of polydispersity ($\sigma < 10\%$, Fig. 1b) obtained for this synthesis, the NP system can be considered as monodisperse [30]. MNPs behave as a magnetic monodomain below a certain critical diameter, usually around 10–20 nm, and exhibit a superparamagnetic behavior. Thus, individual NPs have a large constant magnetic moment and behave like a giant paramagnetic atom with a quick response to applied magnetic fields. These characteristics make the superparamagnetic NPs very attractive for a wide range of applications, such as in the biomedical field, owing to the size of the NPs being compatible with that of biological agents, such as cells [31].

3.3. *Film characterization*

3.3.1. *SEM–EDX*

SEM images of the surfaces of the FC and hybrid films ($FCFe_{0.5}$, $FCFe_{1.4}$, and $FCFe_{3.0}$) are shown in Fig. 2, together with their respective EDX spectra.

The SEM images of the FC (control sample, Fig. 2a) and hybrid films (Fig. 2b–d) showed a fibrous structure on their surfaces. These structures were probably formed from the cellulose chain aggregates, which further self-organized during the removal of the solvent from the films, forming fibrous structures. The surface morphology of the hybrid films ($FCFe_{0.5}$, $FCFe_{1.4}$, and $FCFe_{3.0}$) were similar to that of the FC, suggesting that the introduction of Fe_3O_4 NPs in the cellulosic matrix at concentrations of 0.5, 1.4, and 3.0 g L^{-1} did not affect the surface morphology of the cellulose films.

The EDX spectra of the hybrid films (Fig. 2b–d) indicated the presence of C, O (from cellulose chains), and Fe in these films, which shows that Fe_3O_4 NPs at different concentrations were efficiently incorporated into the cellulosic matrix during its dissolution in DMAc/LiCl. The NPs remained impregnated in the cellulosic matrix after the formation of the films, and were not removed by washing with water, which indicates strong cellulose–magnetite interactions. In addition to the C, O, and Fe, Al and Si were detected in the hybrid film $FCFe_{1.4}$ (Fig. 2c), which are also present in the control film (FC). Silica (SiO_2) represents the major inorganic portion of the ash in higher plants. Behera et al. [32] reported an ash content of 1.27% for sisal, indicating a very low content of Si in this fiber. The presence of aluminum may be due to residues of the processing.

Fig. 3 displays the cross-section SEM images of the films. The cross section of the FC (Fig. 3a) was more homogeneous than those of the hybrid films (Fig. 3b–d). When Fe_3O_4 NPs were present in the cellulosic matrix, the cross section of the films showed that there was a greater distance from the cellulose microfibers (shown by arrows) and, consequently, an increase in the thickness of the films (Fig. 3b–d) compared to the FC (Fig. 3a).

3.3.2. *XRD*

In the XRD image of the FC (Fig. 4a) the typical diffraction pattern of the polymorphic form attributed to cellulose II (mercerized pulp) [1–5], with reflections at 2θ values of 22°, 20°, and 13° corresponding to the (002), (101), and ($10\bar{1}$) planes, respectively, can be observed [33]. Besides the diffraction peaks of crystal cellulose II, hybrid films display distinct peaks that are

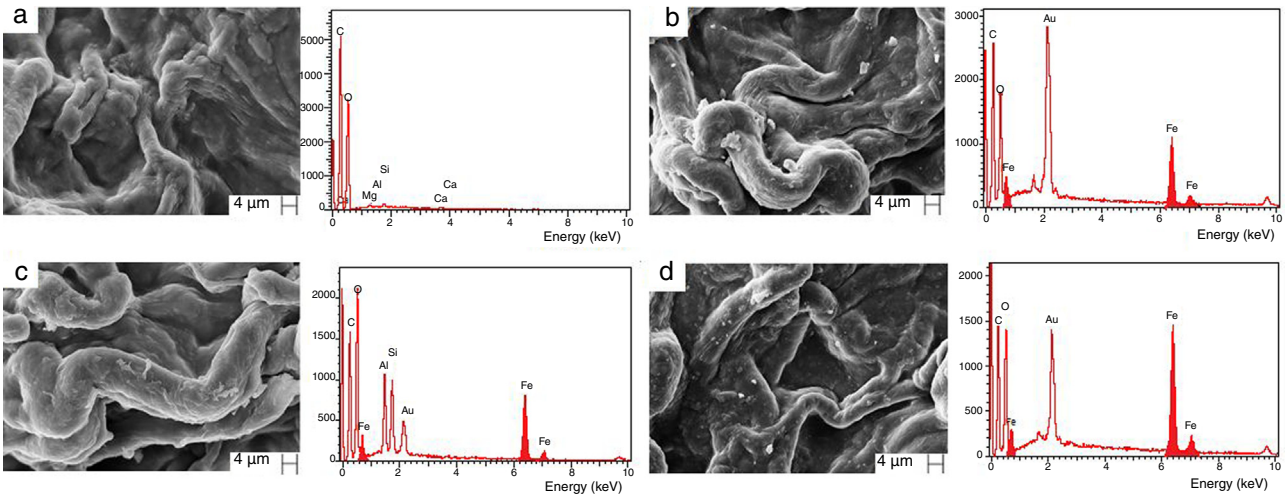

Fig. 2 – SEM micrographs of the surfaces of the films and the respective EDX spectrum, acquired from SEM images of (a) FC, (b) $FCFe_{0.5}$, (c) $FCFe_{1.4}$, and (d) $FCFe_{3.0}$.

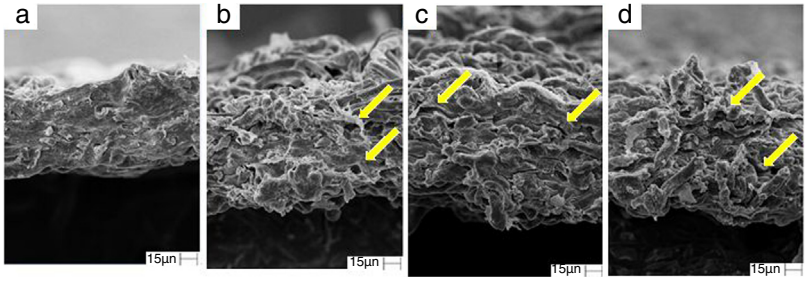

Fig. 3 – SEM micrographs of the cross section of the films: (a) FC, (b) $FCFe_{0.5}$, (c) $FCFe_{1.4}$, and (d) $FCFe_{3.0}$.

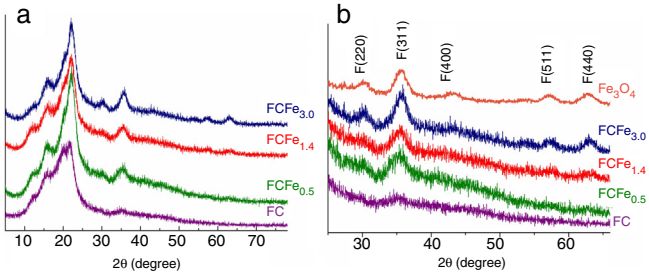

Fig. 4 – XRD patterns of the films (a) obtained with a scanning angle from 5° to 80° in 2θ; (b) amplification of the region corresponding to the diffraction of magnetite (Fe_3O_4).

characteristic of the crystallographic structure of the inverse spinel of magnetite. As expected, the relative intensity of the magnetite diffraction increased with NP concentration in the hybrid film, as indicated in the amplified range region in Fig. 4b. As shown in Fig. 4b, in the film containing the highest concentration of magnetite ($FCFe_{3.0}$), we observed reflections of magnetite at 2θ values of 30.5°, 35.8°, 43.2°, 57.6°, and 63.0° (Joint Committee on Powder Diffraction Standards, JCPDS, card no. 19-629), assigned to the (220), (311), (400), (511), and (440) planes, respectively. In all hybrid film samples, the XRD reflections from magnetite were broadened, in agreement with the nanometer size shown in the TEM analysis. Therefore, magnetic Fe_3O_4 NPs were satisfactorily incorporated into the cellulose in the preparation of the films and were not removed after thorough washing with water, which indicates a strong cellulose–magnetite interaction.

The cellulosic matrix of the $FCFe_{0.50}$, $FCFe_{1.4}$, and $FCFe_{3.0}$ hybrid films exhibited a larger proportion of crystalline regions (Fig. 4), of 70.0%, 64.0%, and 72.0%, respectively, than that of the neat film (FC, 60.0%), indicating that the presence of magnetite NPs favored the formation of cellulose-chain crystalline domains.

3.3.3. *TEM*

The $FCFe_{0.5}$, $FCFe_{1.4}$, and $FCFe_{3.0}$ hybrid films analyzed by TEM were prepared directly on the copper sample holder, which eliminated the need to use an ultramicrotome to cut the films. To confirm the presence of NPs, the TEM images were obtained from the hybrid films and the distribution of NPs was also evaluated qualitatively in the cellulosic matrix. Fig. 5 shows the TEM images for the $FCFe_{0.5}$ and $FCFe_{1.4}$ hybrid films, and the TEM images for the $FCFe_{3.0}$ (not shown) was similar to that of $FCFe_{1.4}$. The observed dark regions (Fig. 5c) may be a consequence of NP agglomeration, which may have been facilitated by the formation of the films analyzed via TEM directly on the reduced size surface of the sample support. Nonetheless, the NPs are well dispersed in most of the image shown (Fig. 5c),

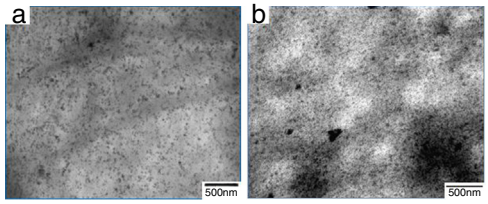

Fig. 5 – TEM images of the hybrid films: (a) $FCFe_{0.5}$ and (b) $FCFe_{1.4}$.

Table 2 – Temperatures of the thermal decomposition of FC, $FCFe_{0.5}$, $FCFe_{1.4}$, and $FCFe_{3.0}$.

Sample	Second step[a]				Fe_3O_4 weight (wt%)[b]
	Weight loss (T_i to T_f) (%)	T_i (°C)	T_f (°C)	T_d (°C)	
FC	66	294	392	355	–
$FCFe_{0.5}$	63	272	363	343	1.3
$FCFe_{1.4}$	61	276	362	343	4.1
$FCFe_{3.0}$	56	280	365	343	6.8

[a] N_2 atmosphere: T_i, initial temperature; T_f, final temperature; T_d, temperature of maximum rate of weight loss.
[b] From TGA performed in air atmosphere (figures not shown).

as they were coated with oleic acid and oleylamine to avoid agglomeration.

3.3.4. TGA

Fig. 6 shows the thermogravimetric (TG) and differential TG (DTG) curves of the control film (FC) and of the hybrid films.

Table 2 summarizes the TGA data derived from the TG and DTG curves (Fig. 6). It also shows the magnetite content, in weight percentage with respect to cellulose, which was determined using TGA in air atmosphere (Section 2.3, figures not shown), because in this condition the percentage of the residue is indicative of the amount of magnetite incorporated into the film. It should be noted that the values shown in Table 2 correspond to the weight percentage of magnetite NPs related to the total weight of the film, whereas 0.5, 1.4, and 3.0 correspond to the concentration ($g\,L^{-1}$) of NPs dispersed in LiCl/DMAc during the preparation of the film.

The TG curves (Fig. 6) of the raw material, FC, and the three hybrid films ($FCFe_{0.5}$, $FCFe_{1.4}$, and $FCFe_{3.0}$) showed three stages of weight loss. The low amount of DMAc in the films, associated to their boiling point (about 160 °C), indicates that the first step of weight loss observed in the films' TGA should be attributed mainly to humidity, and not to DMAc, according to the results presented of the elemental analysis (Table 1). The second step corresponds to the main decomposition of cellulose, leading to levoglucosan, which is produced by the scission of the 1,4-glucosidic linkage in cellulose, followed by the intramolecular rearrangement of the monomer units [34]. This was observed for cellulose and FC from 280 to 400 °C.

It can be seen from Fig. 6a that in the TG curves obtained for the hybrid films the second step of weight loss started at a lower temperature compared to FC (Table 2). FC exhibited a T_d (the temperature of maximum rate of weight loss) of approximately 355 °C, and the presence of magnetite slightly shifted T_d to a lower temperature (Fig. 6b).

3.3.5. Tensile properties

The tensile strength and elongation at break (%) of the control FC and its hybrid films with different concentrations of magnetite were evaluated using experimental stress–strain curves (not shown). The FC exhibited tensile strength and percentage elongation at break values of 9.9 ± 0.1 MPa and 0.66 ± 0.07%, respectively. The hybrid film with the lower concentration of magnetite ($FCFe_{0.5}$) showed values close to those of FC (9.6 ± 0.5 MPa and 0.68 ± 0.01%). The films prepared with higher concentrations of magnetite, $FCFe_{1.4}$ and $FCFe_{3.0}$, showed higher tensile strength and elongation than $FCFe_{0.5}$ and the FC. The tensile strength and elongation of $FCFe_{1.4}$ were 14.3 ± 1.2 MPa and 1.1 ± 0.2%, and for $FCFe_{3.0}$ were 12.1 ± 0.6 MPa and 1.55 ± 0.05%, respectively. These results indicate that the increase of NP concentration in the cellulosic matrix favored sliding between the cellulose chains, thereby facilitating the stretching of the films during stress.

The low percentage of elongation shown by the films characterizes them as rigid, which is a consequence of the low flexibility of the cellulose chains, of the strong intermolecular hydrogen bonds between the hydroxyl groups, and of their high Ic (between 60.0% and 72.0%, as mentioned). The moduli of elasticity are shown in Fig. 7.

The moduli of elasticity of the hybrid films $FCFe_{0.5}$, $FCFe_{1.4}$, and $FCFe_{3.0}$ were 1650 ± 160 MPa, 1500 ± 190 MPa, and 780 ± 100 MPa, respectively, and that of the FC was 1860 ± 280 MPa. These results indicate a tendency of the modulus to decrease from FC to $FCFe_{1.4}$ and a significant decrease

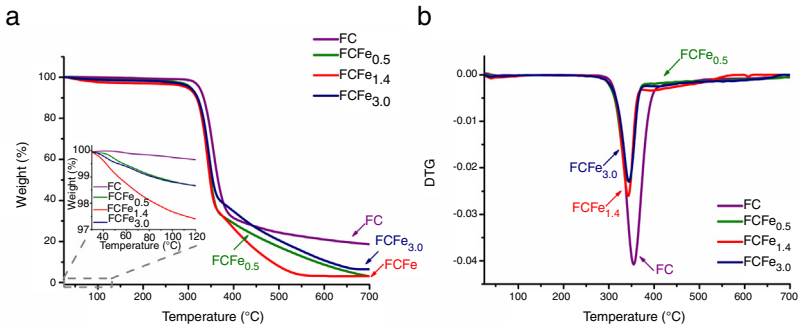

Fig. 6 – (a) TG (insert: magnification from 25 °C to 120 °C) and (b) DTG curves of the control film (FC) and its hybrid films ($FCFe_{0.5}$, $FCFe_{1.4}$, and $FCFe_{3.0}$) (N_2 atmosphere, 50 mL min^{-1}).

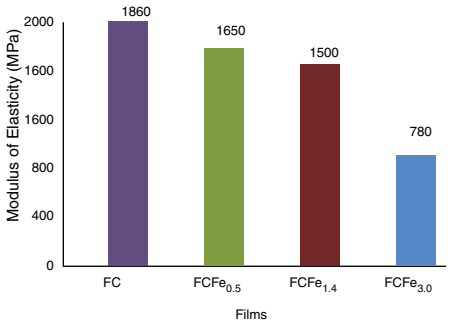

Fig. 7 – Modulus of elasticity for the FC and its hybrid films, $FCFe_{0.5}$, $FCFe_{1.4}$, and $FCFe_{3.0}$.

in this property for $FCFe_{3.0}$. The incorporation of magnetite NPs in the cellulosic matrix provided lower stiffness to the hybrid films compared to the FC (Fig. 7). Although the presence of NPs has favored the formation of crystalline domains, as mentioned, the results of elongation and modulus indicated that the presence of NPs among the cellulose chains had gradually decreased the resistance to deformation of the films.

3.3.6. *Magnetic properties*

Fig. 8a shows the magnetization curve of the magnetite as a function of the applied magnetic field, obtained by the SQUID technique. The analyses were performed at two different temperatures, 5 K and 300 K, in order to evaluate the magnetic behavior of magnetite NPs as a function of temperature.

The hysteresis loop of the magnetite NPs as a function of the applied magnetic field in a range from −70 kOe to 70 kOe showed that the saturation magnetization (M_s; where all the magnetic moments of the materials remain aligned in the applied magnetic field direction) values at 5 K and 300 K (room temperature) are 68.0 and 58.0 emu g^{-1}, respectively (Fig. 8a). These values are lower than that of the saturation magnetization of bulk magnetite and maghemite (dimensions greater than nanometer scale), 92.0 emu g^{-1} and 82.0 emu g^{-1}, respectively, as reported in the literature [35]. This is due to the fact that the contribution to the magnetization from the outermost layers of the material is small owing to the disorganization of the magnetic moments of the surface atoms (surface anisotropy), which promotes the formation of a magnetically inactive layer on the surface of the particles (dead surface layer). A similar behavior has been already reported in the literature [36–38].

The magnification of the magnetization curves around the central region, shown in the inset of Fig. 8a, showed that at 300 K, the magnetite presented a remnant magnetization (M_r; residual magnetization of the material when the external magnetic field is removed) equal to 0.6 emu g^{-1} and the coercivity (H_c; field intensity necessary to override the remanent magnetization) reaches 26 Oe. This field is associated to the remanence of the superconductor magnet used in the MPMS3 SQUID magnetometer.

The very low coercivity and almost zero remanent magnetization values indicate that the magnetite synthesized in this study has a superparamagnetic behavior at room temperature, with absence of magnetic hysteresis. At 5 K, the magnetite showed a blocked superparamagnetic behavior, with a slight opening of the hysteresis loop, showing H_c and M_r values of around 50.0 Oe and 4.0 emu g^{-1}, respectively (Fig. 8a). These results were confirmed by ZFC and field-cooling curves (Fig. 8b), which were obtained to characterize the superparamagnetic behavior of the NPs, as well as to determine their blocking temperature, T_B (the temperature from which the

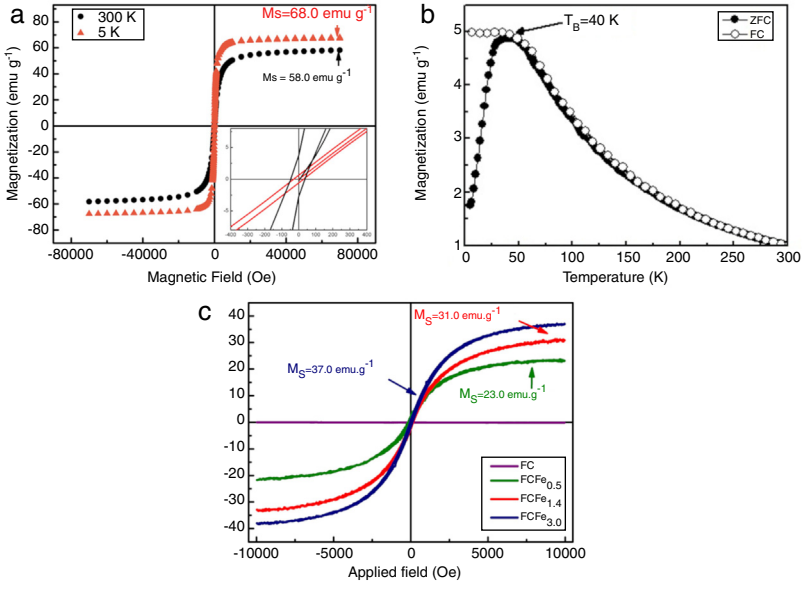

Fig. 8 – (a) Magnetization versus applied magnetic field of magnetite at different temperatures (5 K and 300 K). Inset: amplification of the magnetization curve in the region of low external field (−400 to 400 Oe); (b) zero-field cooling (ZFC) and field-cooling (FC) curves for magnetite NPs, obtained by applying an external magnetic field of 50 Oe; (c) magnetization curves of the FC, $FCFe_{0.5}$, $FCFe_{1.4}$, and $FCFe_{3.0}$ films at 300 K as a function of applied external field parallel to the film surfaces (g: mass of Fe_3O_4 in the films, determined by TGA in air).

thermal fluctuations of the magnetization are destabilized or unblocked).

In order to obtain the ZFC curve, the sample's temperature is first lowered slowly without any external magnetic field, until a low temperature below the blocking temperature (for superparamagnetic materials). Then, a small magnetic field (usually of the order of tens of Oersteds) is applied to the sample, and the magnetization of the system is monitored as a function of the increase in the temperature, keeping the field fixed throughout the measurement. Unlike the ZFC curve, the field-cooling curve is obtained by measuring the magnetization while the sample is cooled below its critical temperature in the presence of an applied external magnetic field [31,39].

The ZFC/field-cooling curves between 5 and 300 K showed that from 40 K, the two curves coincide and separate below the quoted temperature. Thus, 40 K was found to be the blocking temperature for the magnetite NPs synthesized in this study (Fig. 8b). It can be observed that the maximum ZFC curve coincides with the T_B value, which is normally observed for the ZFC/field-cooling curves for superparamagnetic NPs [40].

Above the blocking temperature, in this case $T_B = 40$ K, the NPs have enough energy to overlap the anisotropic energy barrier, i.e., the required energy to revert the magnetization from one stable state to another and become superparamagnetic and unblocked (their magnetic moment varies with the time of the magnetic measurement). This behavior is in accordance with the magnetization curves as a function of the applied magnetic field (Fig. 8a), where H_c and M_r at 300 K have almost zero values because 300 K is above the T_B for magnetite (40 K), where the NPs have superparamagnetic behavior. However, at 5 K, a slight opening of the hysteresis loop of the NPs and a superparamagnetic unblocked behavior are observed because the temperature of the analysis (5 K) is lower than T_B (40 K). Superparamagnetic NPs are very attractive for a wide range of biomedical applications, mainly because aggregation of the particles is avoided when the external magnetic field is removed owing to the magnetization of superparamagnetic NPs disappearing because the magnetic moment remains randomly oriented like in a paramagnetic material, favoring the stability of the NPs [40].

The magnetization curves as a function of applied external field parallel to the film surfaces of the FC and of the hybrid films are shown in Fig. 8c.

The control film (FC), which did not contain a magnetic component in its composition, behaved as a diamagnetic material, as expected, and did not contribute to the magnetization of the sample in the presence of the applied external field (Fig. 8c). Because the magnetization is expressed in electromagnetic units per units of mass of the analyzed material, the magnetization curves of the hybrid films were obtained considering the magnetite mass contained in the portion of the film analyzed (determined by TGA in air) to be 1.3%, 4.1%, and 6.8% in the $FCFe_{0.5}$, $FCFe_{1.4}$, and $FCFe_{3.0}$ films, respectively (Table 2). The total mass of the film evaluated was not considered in this work because the cellulose is diamagnetic, as mentioned. Thus, if the total mass was considered in the magnetization calculations, the cellulose present would contribute to the mass increase, but would not contribute to the magnetization, and the saturation magnetization (M_s) values for the films would be underestimated.

It was observed that the (M_s) of the hybrid films increased with the concentration of magnetite NPs dispersed in the films, as expected. High magnetizations for the hybrid films were obtained at room temperature, corresponding to 23.0 emu g^{-1} for $FCFe_{0.5}$, 31.0 emu g^{-1} for $FCFe_{1.4}$, and 37.0 emu g^{-1} for $FCFe_{3.0}$ (Fig. 8c).

The M_s values of the hybrid films were lower than that of the neat NPs (58.0 emu g^{-1}, at 300 K; Fig. 8a); i.e., the magnetic response of the magnetite NPs in the films to the application of an external field was lower than that of the neat NPs, which may be attributed to the fact that the magnetic NPs in the films are surrounded by the diamagnetic cellulose matrix. Hybrid films showed no magnetic hysteresis at 300 K and zero remnant magnetization (M_r) and, therefore, behaved as superparamagnetic materials at room temperature.

4. Conclusions

Sisal cellulose/magnetite-nanoparticle hybrid films containing three different nanoparticle concentrations were successfully prepared by a casting method. The possibility of using underivatized cellulose represents an advantage because it eliminates the cost involved in the derivatization reaction.

The hydrophobic magnetic nanoparticles with an average diameter of 5 nm were synthesized by the modified polyol process. After purification methodology, the nanoparticles remain coated with a mixture of oleic acid and oleylamine onto the surface that favors their dispersion in the film medium preparation avoiding significant nanoparticles aggregation.

The presence of the magnetic nanoparticles into the hybrid films influenced their mechanical properties. FCFe1.4 and FCFe3.0 exhibited higher tensile strengths (14.3 MPa and 12.1 MPa, respectively) than the neat cellulose film (9.9 MPa). The moduli of elasticity of FCFe0.5, FCFe1.4, and FCFe3.0 were 1650, 1500 MPa, and 780 MPa, respectively, lower than that of the cellulose film (1860 MPa), indicating that the incorporation of nanoparticles in the cellulosic matrix decreased the films' stiffness.

Hybrid films exhibited high magnetizations at 300 K with values of 23.0 emu g^{-1} (FCFe0.5), 31.0 emu g^{-1} (FCFe1.4), and 37.0 emu g^{-1} (FCFe3.0), as well as the superparamagnetic behavior at room temperature. The results showed that hybrid films with useful properties, including magnetization, can be obtained from cellulose and magnetite.

The properties of the bio-based nanocomposites prepared in the present study point to a wide range of possible applications, such as in sensors, micromechanical devices, advanced catalysis, and biomedical applications, among others. In addition, the methodology can also be easily adjusted to promote the incorporation of different hydrophobic nanoparticles in the cellulose matrix, conferring new properties such as optical and electronic ones.

Conflicts of interest

There are no conflicts to declare.

Acknowledgements

The authors would like to thank CAPES (Coordination for the Improvement of Higher Level or Education Personnel) for providing a fellowship for D.M.F., as well as CNPq (National Council of Scientific Research) for a research productivity fellowship to E.F. and for financial support (Process 426847/2016-4), as well as FAPESP (State of São Paulo Research Foundation, Brazil) for financial support (Process 2012/00116-6 and 2013/01284-2, 2009/54082-2, 2013/07296-2).

REFERENCES

[1] Ramos LA, Assaf JM, El Seoud OA, Frollini E. Influence of the supramolecular structure and physicochemical properties of cellulose on its dissolution in a lithium chloride/N,N-dimethylacetamide solvent system. Biomacromolecules 2005;6(5):2638–47.
[2] Kaschuk JJ, Frollini E. Effects of average molar weight, crystallinity, and hemicelluloses content on the enzymatic hydrolysis of sisal pulp, filter paper, and microcrystalline cellulose. Ind Crops Prod 2018;115:280–9.
[3] Rodrigues BVM, Heikkilä E, Frollini E, Fardim P. Multi-technique surface characterization of bio-based films from sisal cellulose and its esters: a FE-SEM, μ-XPS and ToF-SIMS approach. Cellulose 2014;21(3):1289–303.
[4] Almeida EVR, Morgado DL, Ramos LA, Frollini E. Sisal cellulose and its acetates: generation of films and reinforcement in a one-pot process. Cellulose 2013;20(1):453–65.
[5] Morgado DL, Martins VCA, Plepis AMDG, Frollini E. Aggregation of chains of cellulose acetates in LiCl/DMAc: evaluation via viscometry. Polím Ciênc Tecnol 2011;21(2):143–5.
[6] Klemm D, Heublein B, Fink H-P, Bohn A. Cellulose: fascinating biopolymer and sustainable raw material. Angew Chem Int Ed English 2005;44(22):3358–93.
[7] Phinichka N, Kaenthing S. Regenerated cellulose from high alpha cellulose pulp of steam-exploded sugarcane bagasse. J Mater Res Technol 2018;7(1):55–65.
[8] Courtenay JC, Ramalhete SM, Skuze WJ, Soni R, Khimyak YZ, Edler KJ, et al. Unravelling cationic cellulose nanofibril hydrogel structure: NMR spectroscopy and small angle neutron scattering analyses. Soft Matter 2018;14(2):255–63.
[9] Kaufman G, Mukhopadhyay S, Rokhlenko Y, Nejati S, Boltyanskiy R, Choo Y, et al. Highly stiff yet elastic microcapsules incorporating cellulose nanofibrils. Soft Matter 2017;13(15):2733–7.
[10] Aguilera LS, Marçal RLSB, Campos JB, Silva MHP, Figueiredo AB-HS. Magnetic filter produced by $ZnFe_2O_4$ nanoparticles using freeze casting. J Mater Res Technol 2018:350–5.
[11] Sanchez PA, Gundermann T, Dobroserdova A, Kantorovich SS, Odenbach S. Importance of matrix inelastic deformations in the initial response of magnetic elastomers. Soft Matter 2018;14(11):2170–83.
[12] Liu S, Zhou J, Zhang L, Guan J, Wang J. Synthesis and alignment of iron oxide nanoparticles in a regenerated cellulose film. Macromol Rap Commun 2006;27(24):2084–9.
[13] Zhou J, Li R, Liu S, Li Q, Zhang L, Zhang L, et al. Structure and magnetic properties of regenerated cellulose/Fe_3O_4 nanocomposite films. J Appl Polym Sci 2008;111(5):2477–84.
[14] Liu S, Zhou J, Zhang L. In situ synthesis of plate-like Fe_2O_3 nanoparticles in porous cellulose films with obvious magnetic anisotropy. Cellulose 2011;18(3):663–73.
[15] Wang F, Yang Y, Ling Y, Liu J, Cai X, Zhou X, et al. Injectable and thermally contractible hydroxypropyl methyl cellulose/Fe_3O_4 for magnetic hyperthermia ablation of tumors. Biomaterials 2017;128:84–93.
[16] Spiridonov VV, Panova IG, Makarova LA, Afanasov MI, Zezin SB, Sybachin AV, et al. The one-step synthesis of polymer-based magnetic γ-Fe_2O_3/carboxymethyl cellulose nanocomposites. Carbohydr Polym 2017;177:269–74.
[17] Pinto RJB, Neves MC, Neto CP, Trindade T. Composites of cellulose and metal nanoparticles. In: Ebrahimi F, editor. Nanocomposites – new trends and developments. Rijeka, Croatia: InTech; 2012. p. 73–96.
[18] Liu K, Nasrallah J, Chen L, Huang L, Ni Y. Preparation of CNC-dispersed Fe_3O_4 nanoparticles and their application in conductive paper. Carbohydr Polym 2015;126:175–8.
[19] Qin Y, Qin Z, Liu Y, Cheng M, Qian P, Wang Q, et al. Superparamagnetic iron oxide coated on the surface of cellulose nanospheres for the rapid removal of textile dye under mild condition. Appl Surf Sci 2015;357:2103–11.
[20] Xiong R, Lu C, Wang Y, Zhou Z, Zhang X. Nanofibrillated cellulose as the support and reductant for the facile synthesis of Fe_3O_4/Ag nanocomposites with catalytic and antibacterial activity. J Mater Chem A 2013;1(47):14910–8.
[21] Li Y, Zhu H, Gu H, Dai H, Fang Z, Weadock NJ, et al. Strong transparent magnetic nanopaper prepared by immobilization of Fe_3O_4 nanoparticles in a nanofibrillated cellulose network. J Mater Chem A 2013;1(48):15278.
[22] Zhang H, Zheng JY. Immobilization of magnetic magnetite nanoparticle film on polyamide fabric. J Appl Polym Sci 2012;125(5):3770–7.
[23] Figuerola A, Di Corato R, Manna L, Pellegrino T. From iron oxide nanoparticles towards advanced iron-based inorganic materials designed for biomedical applications. Pharmacol Res 2010;62(2):126–43.
[24] Shim IW, Choi S, Noh WT, Kwon J, Cho JY, Chae DY, et al. Preparation of iron nanoparticles in cellulose acetate polymer and their reaction chemistry in the polymer. Bull Korean Chem Soc 2001;22(7):772–4.
[25] Lacerda TM, Zambon MD, Frollini E. Effect of acid concentration and pulp properties on hydrolysis reactions of mercerized sisal. Carbohydr Polym 2013;93(1):347–56.
[26] Morgado DL, Rodrigues BVM, Almeida EVR, El Seoud OA, Frollini E. Bio-based films from linter cellulose and its acetates: formation and properties. Materials 2013;6(6):2410–35.
[27] Ramos LA, Morgado DL, El Seoud OA, Silva VC, Frollini E. Acetylation of cellulose in LiCl-N,N-dimethylacetamide: first report on the correlation between the reaction efficiency and the aggregation number of dissolved cellulose. Cellulose 2011;18(2):385–92.
[28] Souza CGS, Beck W, Varanda LC. Multifunctional luminomagnetic FePt@Fe_3O_4/SiO_2/Rhodamine B/SiO_2 nanoparticles with high magnetic emanation for biomedical applications. J Nanopart Res 2013;15(4):1545.
[29] Varanda LC, Imaizumi M, Santos FJ, Jafelicci M. Iron oxide versus Fe55Pt45/Fe_3O_4: improved magnetic properties of core/shell nanoparticles for biomedical applications. IEEE Trans Magnet 2008;44(11):4448–51.
[30] Hunter R. Foundations of colloid science. 2nd ed. Oxford: Oxford University Press; 2001.
[31] Lu AH, Salabas EL, Schüth F. Magnetic nanoparticles: synthesis, protection, functionalization, and application. Angew Chem Int Ed 2007;46(8):1222–44.
[32] Behera S, Patel S, Mishra BK. Effect of blending of sisal on pulp properties of waste papers in handmade papermaking. J Scient Ind Res 2015;74:416–22.
[33] Ass BAP, Ciacco GT, Frollini E. Cellulose acetates from linters and sisal: correlation between synthesis conditions in

DMAc/LiCl and product properties. Bioresource Technol 2006;97(14):1696–702.
[34] Li Y, Mai YW, Ye L. Sisal fibre and its composites: a review of recent developments. Compos Sci Technol 2000;60(11):2037–55.
[35] Cornell RM, Schwertmann U. The iron oxides: structure, properties, reactions occurences and uses. New York: Wiley-VCH; 2003.
[36] Morales MP, Veintemillas-Verdaguer S, Montero MI, Serna CJ, Roig A, Casas L, et al. Surface and internal spin canting in γ-Fe_2O_3 nanoparticles. Chem Mater 1999;11(11): 3058–64.
[37] Correa JR, Bordallo E, Canetti D, León V, Otero-Díaz LC, Negro C, et al. Structure and superparamagnetic behaviour of magnetite nanoparticles in cellulose beads. Mater Res Bull 2010;45(8):946–53.
[38] Souza JB, Varanda LC. Magneto-plasmonic Au-coated Co nanoparticles synthesized via hot-injection method. Nanotechnology 2018;29(6):065604.
[39] Cullity BD, Graham CD. Introduction to magnetic materials. 2nd ed. Wiley-IEEE Press; 2009.
[40] Altavilla C, Ciliberto E. Inorganic nanoparticles: synthesis applications and perspectives. 1st ed. Boca Raton: CRC Press; 2011.